Acta Materialia 166 (2019) 371–385

Contents lists available at ScienceDirect

Acta Materialia

journal homepage: www.elsevier.com/locate/actamat

Full length article

Fabrication of high-quality Ti joint with ultrafine grains using submerged friction stirring technology and its microstructural evolution mechanism

L.H. Wu, X.B. Hu, X.X. Zhang, Y.Z. Li, Z.Y. Ma**, X.L. Ma, B.L. Xiao*

Shenyang National Laboratory for Materials Science, Institute of Metal Research, Chinese Academy of Sciences, 72 Wenhua Road, Shenyang, 110016, China

ARTICLE INFO

Article history:
Received 9 July 2018
Received in revised form
22 November 2018
Accepted 31 December 2018
Available online 3 January 2019

Keywords:
Friction stir
Titanium
Recrystallization
Deformation
Finite element simulation

ABSTRACT

It is rather challenging to obtain high-quality Ti joints by conventional friction stir welding because of the problem of over-heating. The welding process and final microstructures and properties of the joints are controlled by both plastic deformation and recrystallization. However, for a long time, studies have only focused on recrystallization mechanisms but ignored deformation modes. In this study, a defect-free ultrafine-grained Ti joint with a joint efficiency of 100% was for the first time produced by submerged friction stirring (SFS) technology. We utilized transmission electron microscopy with a two-beam diffraction technique and electron backscatter diffraction to systematically investigate the deformation mode versus the grain refinement mechanism. The finite element method was utilized to simulate the temperature field throughout the joint for the microstructural explanation. During the whole SFS, prismatic slip occurred, and the other dominant deformation mechanisms changed from $\{10\bar{1}2\}$ twinning and basal slip to pyramidal <a + c> slip. The variation of slip modes was largely dependent on the twinning and temperature rise. The ultrafine-grained microstructure was attributed to the successive refinement effect of the twin-dislocation interaction, dislocation absorption, dynamic grain boundary migration and texture-induced grain convergence. The effect of the temperature, strain and strain rate on the microstructural evolution mechanisms was discussed. Based on our work, we expect the wide application of SFS in producing ultrafine-grained bulk Ti materials and high-quality joints.

1. Introduction

Friction stir welding (FSW), a solid-state joining technique, can produce high-quality joints, and has been widely studied and applied for various metals, composites and even polymers [1–3]. Friction stir processing (FSP), based on the basic principle of FSW, is usually used to refine the microstructure [1]. Recently, friction stirring (FS), including FSW and FSP, was performed under fluid coolant to adjust the heat distribution, and this was called submerged friction stirring (SFS) [4,5]. It was reported that SFS could significantly increase the joint strength by reducing the extent of softening of the heat-affected zone [6]. In addition, a large-area bulk ultrafine-grained Al material has been produced by SFS [7]. Benefiting from these advantages, SFS is nowadays gradually becoming a very important technology to achieve sound joints and produce ultrafine-grained materials.

As we know, FS/SFS involves both plastic deformation and dynamic recrystallization (DRX), and thus the deformation mode and DRX concurrently determine the FS/SFS process and the final microstructure and properties of the joints. Besides, plastic deformation combined with thermal exposure during FS/SFS induces the operation of DRX. Therefore, the deformation mode itself has a significant influence on the DRX mechanisms. However, for a long time, researchers just put a high emphasis on the DRX mechanisms but ignored the deformation modes [8,9], because of the difficulty in directly identifying deformation modes, resulting in one-sided conclusions on the microstructural evolution mechanisms. Some studies simply regarded the easy slip system of metals as the main deformation modes during FS, based on the inference of very preliminary microstructure features [10]. However, in many cases, the activated deformation modes are far more complicated than the easy slip systems, since they are significantly influenced by the

* Corresponding author.
** Corresponding author.
E-mail addresses: lhwu@imr.ac.cn (L.H. Wu), xbhu@northwestern.edu (X.B. Hu), xxzhang@imr.ac.cn (X.X. Zhang), yzli@alum.imr.ac.cn (Y.Z. Li), zyma@imr.ac.cn (Z.Y. Ma), xlma@imr.ac.cn (X.L. Ma), blxiao@imr.ac.cn, blxiao@imr.ac.cn (B.L. Xiao).

https://doi.org/10.1016/j.actamat.2018.12.059
1359-6454/

deformation conditions (e.g. strain, strain rate and temperature), especially temperature [11,12].

For example, for α-Ti with a hexagonal close packed (HCP) structure, prismatic <a> slip ({10$\bar{1}$0} <11$\bar{2}$0>) is the main deformation mode during plastic deformation at room temperature. However, during equal channel angular pressing (ECAP) of Ti at 350 °C, the deformation modes were totally different for different passes. During the first pass, twinning dominated the deformation, while in the second pass the deformation mechanism changed to dislocation slip. Additionally, for the different deformation routes, the slip modes changed among prismatic slip, basal slip ({0002} <11$\bar{2}$0>) and pyramidal <c + a> slip ({10$\bar{1}$1} <11$\bar{2}$3>) [12]. For FS/SFS, they exhibit obvious deformation characteristics associated with rapid transients and steep gradients in temperature, strain and strain rate, and it is very difficult to measure or simulate the exact temperature, strain and strain rate fields [1]. This means that the deformation state and deformation modes for FS/SFS are probably more complex than those for other hot-working techniques. Therefore, revealing the deformation modes during FS/SFS is very fundamental and stringent.

In addition to deformation, the grain refinement mechanism is another key point to control the final microstructure and properties. Large numbers of previous studies [13–15] indicated that the grain refinement mechanism of FCC metals during FS largely depended on the stacking fault energy (SFE). The grain refinement mechanism during FS of FCC metals with a high SFE was usually continuous DRX (CDRX), which was related to the gradual increase of the misorientation angle of subgrains [13]. However, discontinuous DRX (DDRX), associated with a classic nucleation and growth process, was easily operative for metals with a low SFE [15]. Mironov et al. [9] pointed out that the dependence of the DRX mechanism on the SFE was essentially related to the variation of dislocation mobility, since the dislocation mobility was largely dependent on the SFE.

Compared to FCC metals, the grain refinement mechanism of HCP metals during FS has not been well understood, possibly associated with their fewer slip systems, anisotropic slip modes and twinning [9,10,16]. So far, most studies on the grain structure evolution of HCP metals have focused on Mg [8,9,16], which acts as a modeling material with a *c/a* ratio of 1.624, close to the ideal ratio (1.633) for HCP structure, a low SFE (the basal SFE ~25–35 mJ/m^2), and basal slip as the main slip mode [9,11]. Different from Mg, α-Ti has a lower *c/a* value (1.587), a high SFE of >300 mJ/m^3, and prismatic slip as the main slip mode [11], and can be another type of HCP modeling material. However, it is rather challenging to investigate the grain evolution of α-Ti during FS due to the tool wear and high strength, low thermal conductivity and high reactivity for Ti [17–22].

Recently, the DRX process of α-Ti during FS was subjected to investigations [10,17,22]. It was reported that CDRX associated with gradual subgrain rotation was the main grain refinement mechanism of FS Ti-6Al-4V alloy [17]. During FS of pure Ti, the grain evolution was a complex process mainly related to geometrical effects of strain and texture evolution [10]. For SFS, however, materials experience deformation at a much lower temperature compared to that for FS at the same process parameters. Thus, the grain structure evolution during SFS is probably quite different from that during FS. However, so far, there has still been no systematic investigation of the grain structure evolution of HCP metals during SFS.

In this study, pure Ti was used as the experimental modeling material to subject to SFS under flowing water. The deformation mode and grain refinement mechanism of the SFS Ti joint were systematically studied by electron backscatter diffraction (EBSD) and transmission electron microscopy (TEM). The temperature field of the joint simulated by the finite element method was utilized to explain the microstructural phenomenon. We aim to explore the feasibility of SFS for Ti-based materials, clarify the deformation and DRX mechanisms of HCP metals during SFS, and reveal the underlying temperature effects.

2. Experimental procedures and modeling methods

2.1. Experimental section

The as-received materials were 2-mm-thick commercially pure Ti sheets. Prior to welding, the Ti sheets were first fixed under water (with the water level just over the Ti sheets), and then the cyclic flowing water was used to rapidly cool the weld during SFS. SFS was conducted at a rotation rate of 300 rpm and a travel speed of 25 mm/min using a W-5Re tool with a concave shoulder 11 mm in diameter and a pin 1.65 mm in length, tapered from 6 mm at the shoulder with a taper angle of 30°.

Microstructural characterization was carried out by optical microscopy (OM), EBSD (HKL, Channel 5 type) and TEM (JEM-2100, 200 kV). All specimens for OM and EBSD were cut perpendicular to the welding direction. The retreating side was abbreviated as RS. TD, ND and WD indicate the transverse direction, normal direction and welding direction, respectively. Specimens for both EBSD and TEM were prepared by twin-jet electropolishing with a solution of 6 vol % $HClO_4$ + 34 vol % CH_3OH + 60 vol % C_4H_9OH at about −30 °C.

EBSD maps of ~1,500,000 pixels were obtained at a step size of 0.07–0.85 μm. In order to ensure the reliability of the EBSD data, all small grains comprising 3 or fewer pixels were excluded automatically from the maps using an artifact filter tool in the Channel 5 software. A lower limit boundary misorientation cut-off of 2° was used to eliminate the spurious boundaries resulting from the orientation noise. A critical angle of 15° was used to define the low angle grain boundary (LAGB) and high angle grain boundary (HAGB). The spacings of the LAGBs and HAGBs were measured with a linear intercept method to describe the subgrain and grain sizes. In the EBSD maps, black, red, green and blue lines represented HAGBs, LAGBs, {10$\bar{1}$2} and {10$\bar{1}$1} twin boundaries (TBs), respectively.

2.2. Finite element simulation

In order to explain the deformation and grain refinement mechanisms, the temperature field of the SFS Ti joint was simulated by a mathematical model. The governing equation for the heat flow of a solid is given by Ref. [23].

$$\rho(T)c(T)\frac{\partial T}{\partial t} = \nabla\cdot[\lambda(T)\nabla T] + q \tag{1}$$

where the temperature-dependent density ρ, heat capacity c and thermal conductivity λ are considered to improve the modeling accuracy; q is the heat generation rate, ∇ the gradient operator, and T the temperature.

The heat generation rate q is defined by

$$q = \mu p\left(\frac{2\pi\omega}{60}r + \frac{\upsilon}{60}\sin\theta\right) \tag{2}$$

where μ is the friction coefficient, p the pressure, ω the rotation rate, υ the advancing speed, and θ the angle between the tool velocity and the welding direction.

During FSW, a significant amount of heat will be transported from the tool to the workpiece. The heat flux on the tool/workpiece interface may be defined via [24].

$$k\frac{\partial T}{\partial z}=\frac{\sqrt{(k\rho c)_W}}{\sqrt{(k\rho c)_W}+\sqrt{(k\rho c)_T}}q \tag{3}$$

where k is the thermal conductivity, and the subscripts W and T denote the workpiece and the tool, respectively.

For the heat exchange between the surfaces and the surroundings, both radioactive and convective heat transfers are taken into account, which indicates

$$-k\frac{\partial T}{\partial z}=\varepsilon\sigma\left(T^4-T_a^4\right)+h_t(T-T_a) \tag{4}$$

where ε is the emissivity, T_a the room temperature, and h_t the heat transfer coefficient.

For the heat exchange between the surfaces, the jigs and the backing plate, the convective heat transfer is considered, which reads

$$k\frac{\partial T}{\partial z}=h_b(T-T_a) \tag{5}$$

where h_b is the heat transfer coefficient.

In the present study, the friction coefficient μ is set to 0.4. The temperatures of the surroundings and backing plate are set to room temperature T_a. The governing equation and the boundary conditions are solved via the finite element method in the software *MSFESL* developed at our laboratory [25].

3. Results

After SFS, a defect-free Ti joint with full penetration was successfully obtained, as shown by the cross-sectional macrostructure in Fig. 1. Three typical zones were identified in the joint, i.e. the stir zone (SZ), the base material (BM) and the narrow transition zone – thermo-mechanically affected zone (TMAZ). The SZ exhibited a parabolic profile with a progressive increment in the width from the bottom to the upper surface, which might be attributed to the influence of the shoulder on the material flow of thin sheets and the taper pin itself [10]. Table 1 shows the tensile properties of the BM and SFS joint. It was clear that the SFS joint showed a high tensile strength of 456 MPa, comparable to the BM, although the ductility decreased. In other words, the joint efficiency was 100%, which suggested that SFS was an effective way to produce high-quality Ti joints. In order to reveal the deformation modes and grain refinement mechanisms during SFS, the microstructural features of the BM, TMAZ and SZ are characterized.

3.1. Base material

The microstructural characteristics of the BM are shown in Fig. 2. The BM consisted of equiaxed grains with an average grain size of 25.7 μm (Fig. 2a). The misorientation angle distribution in Fig. 2b indicated that the fraction of HAGBs was 76.1%. The BM showed a typical rolling texture for α-Ti with a relatively weak texture component with a maximum intensity of 4.6, and two texture peaks were located at the ND and the position deviated from the ND to the TD for ~25°, respectively (Fig. 2c).

Fig. 1. Cross section of SFS Ti joint at rotation rate of 300 rpm and travel speed of 25 mm/min. TD, ND and WD indicate the transverse direction, normal direction and welding direction, respectively.

Table 1
Transverse tensile property of BM and SFS joint of pure Ti.

Materials	Tensile strength, MPa	Elongation, %	Joint efficiency
BM	452	40.7	–
SFS joint	456	21.4	100%

3.2. Thermo-mechanically affected zone

The TMAZ, as the transition zone of the BM and the SZ, is important to understand how the microstructure of the unaffected BM evolves into that of the refined SZ during SFS [10]. A large EBSD map across the TMAZ and a small portion of the SZ taken from the black polygon in Fig. 1 is shown in Fig. 3a. Based on the microstructural characteristics (Fig. 3a), the TMAZ was approximately subdivided into three regions for better understanding the microstructural evolution during SFS. The main subdivision principle in Fig. 3a was listed as follow. The border of TMAZ 1 and TMAZ 2 was marked based on that TBs were significantly reduced and a large number of LAGBs were introduced in TMAZ 2. The border of TMAZ 2 and TMAZ 3 was marked based on that TBs almost disappeared and the fraction of LAGBs increased largely in TMAZ 3. The border of TMAZ 3 and the SZ was marked based on that the grains were refined significantly in the SZ.

In TMAZ 1, a large fraction of 8.7% of $\{10\bar{1}2\}$ TBs (green lines, misorientation angle/axis pair of 85° $<11\bar{2}0>$ with a tolerance of 5°) with a large twin width of ~5–10 μm was introduced into the grains (Fig. 3a). Besides, there was a phenomenon that one boundary consisted of several segments of TBs and random HAGBs, a typical example of which is shown in Fig. 3b. Near the border of the TBs and HAGBs (arrow in Fig. 3b), the misorientation of the HAGB (line F) was similar to that of the TB (line E), both in the range of 85±5° (Figs. 3c and d). However, the misorientation axis of the random HAGB deviated 6° from $<11\bar{2}0>$ (not shown). It was inferred that the random HAGBs likely evolved from the TBs via the variation of the misorientation angle or axis, and this phenomenon was related to a strain-induced twin destruction process [16]. Fig. 3e shows that the misorientation axis of the majority of boundaries within 85±5° was near $<\bar{1}2\bar{1}0>$, suggesting that these boundaries mainly consisted of $\{10\bar{1}2\}$ TBs and random HAGBs originated from the TBs. The total fraction of HAGBs within 85±5° was 26.1%, much larger than that of TBs (8.7%), which suggests that a large fraction of TBs have been transformed into HAGBs by the twin destruction process.

In TMAZ 2, the fraction of TBs obviously decreased but LAGBs (red lines) greatly increased (Fig. 3a). Table 2 showed that the fraction of TBs reduced to only 2.4%, but the fraction of LAGBs increased to 55% as the result of dynamic recovery. In some grains, a TB was even completely transformed into a random HAGB, with an example shown in Fig. 3f. For simplification, these HAGBs transformed from the TBs were called as “T-HAGBs", in order to distinguish from other common HAGBs. Fig. 3h further confirmed that the misorientation of these HAGBs entirely deviated from the standard value (85°) of the TBs, as the result of a further strain-induced twin destruction process. After the TBs were totally transformed to HAGBs, these “T-HAGBs" divided one base grain into several new grains (Figs. 3f and g). The new grain, which was directly transformed by one twin, retained the lens shape of the twin (arrows in Figs. 3f and g). Obviously, the grain boundary angles of this new lens-shaped grain were much less than the equilibrium angle of ~120° (e.g. one was just 22° marked in Fig. 3g). Thus, these “T-HAGBs" were unstable, and they had a strong trend to migrate,

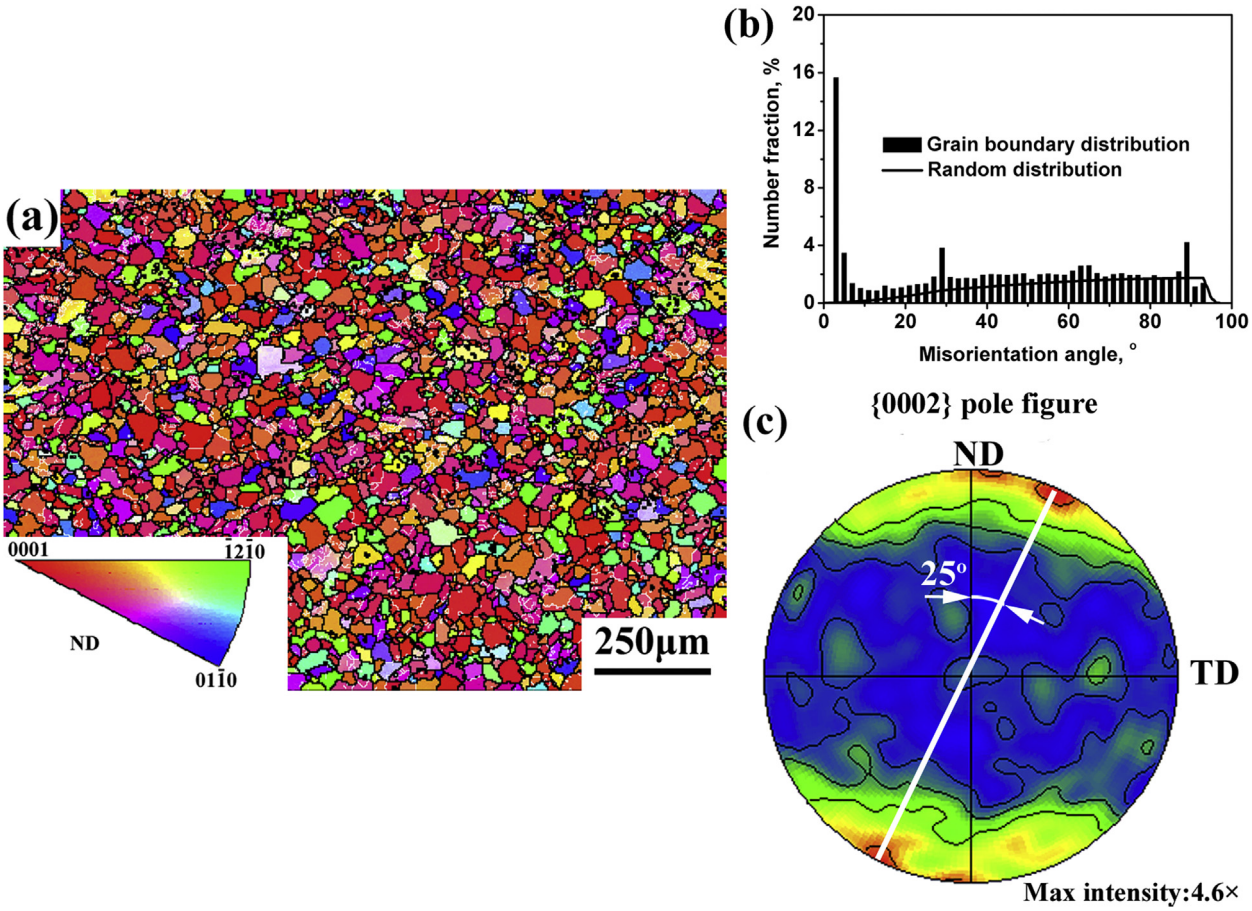

Fig. 2. EBSD maps of BM: (a) orientation map, (b) misorientation angle distribution, and (c) (0002) pole figure in TD-ND reference frame.

in order to form steady grains with equilibrium grain boundary angles.

Also, the phenomenon of the migration of the "T-HAGBs" was observed in TMAZ 2, as shown in Figs. 3i and j. Figs. 3i, j and k confirmed that the misorientation of these "T-HAGBs" (the boundaries I-K in Fig. 3i) has totally deviated from the standard value of 85°<11$\bar{2}$0> (Although the misorientation of the boundaries H and J was still within 85±5°, their misorientation axis was <41$\bar{5}$0> and <44$\bar{8}$3>, respectively, totally deviating from the standard axis of <11$\bar{2}$0>). It was obvious that these straight "T-HAGBs" has evolved into some curve-shaped boundaries of several grains (Figs. 3i and j). As a result, the original base grain was refined into several new grains (the grains O-T in Fig. 3j). Thus, the formation of new grains in TMAZs 1 and 2 was mainly related to twinning, and the main refinement mechanism in these two regions should be attributed to twinning induced DRX (TDRX), which will be discussed in Section 4.2. Some other details on the grain evolution related to TDRX in TMAZs 1 and 2 please refer to Supplementary Fig. S1.

In order to clarify the deformation mechanism in TMAZs 1 and 2, the typical substructure characteristics in these regions were observed by TEM, as shown in Fig. 4. A large number of twins and dislocations were observed, and dislocations existed at twin boundaries or within the twins (Figs. 4a and b). We utilized TEM with the two-beam diffraction technique to clarify the dislocation type. According to the dislocation invisible rule: $\mathbf{g}\times\mathbf{b}=\mathbf{0}$ ($\mathbf{g}$ represents the operating vector and $\mathbf{b}$ represents the Burgers vector), <a> type dislocations ($\mathbf{b}=<1\bar{2}10>$) are visible under the $\mathbf{g}_{10\bar{1}0}$ vector, but invisible under the $\mathbf{g}_{0002}$ vector; <a + c> type ($\mathbf{b}=<1\bar{2}13>$) is visible under the $\mathbf{g}_{0002}$ vector [12,26]. By this rule, the majority of dislocations in TMAZs 1 and 2 were determined to be <a> type (Figs. 4c and d). Also, the tiny minority of <a + c> dislocation loop was observed (the double arrows in Figs. 4c and d).

As we know, when the inclined beam aligned with different directions, dislocations on different slip planes exhibited different morphologies. Therefore, we tilted the foils to confirm the slip plane [26]. The schematic of <a> dislocation morphologies on prismatic and basal planes observed from <0002> and <1$\bar{2}$10> directions is summarized in Fig. 5, and for <a> dislocation characteristics on {10$\bar{1}$1} pyramidal planes please refer to Supplementary Figs. S2 and S3. When observed along the <0002> direction, the prismatic <a> dislocations exhibit straight trace lines or points parallel to the <1$\bar{2}$10> directions, and the trace lines show some widths because of the overlapped effects along <0002> direction. For basal <a> dislocations, their projected length would be longer when observed along the <0002> direction compared to other inclined directions, and they exhibited straight trace lines parallel to <10$\bar{1}$0> with some widths when observed along the <1$\bar{2}$10> direction. Therefore, based on the TEM observations from the <0002> and <1$\bar{2}$10> directions, most of the dislocations in TMAZs 1 and 2 lay on both prismatic and basal planes. The typical dislocations observed from the <0002> direction are shown in Figs. 4e and f, where the prismatic <a> dislocations exhibited the straight trace lines with some widths along the <1$\bar{2}$10> directions (black arrows in Fig. 4e), and the basal <a> dislocations showed a long bending characteristic (Fig. 4f). Therefore, in TMAZs 1 and 2, prismatic and basal <a> slips, as well as {10$\bar{1}$2} twinning are the main deformation mode (Figs. 3 and 4).

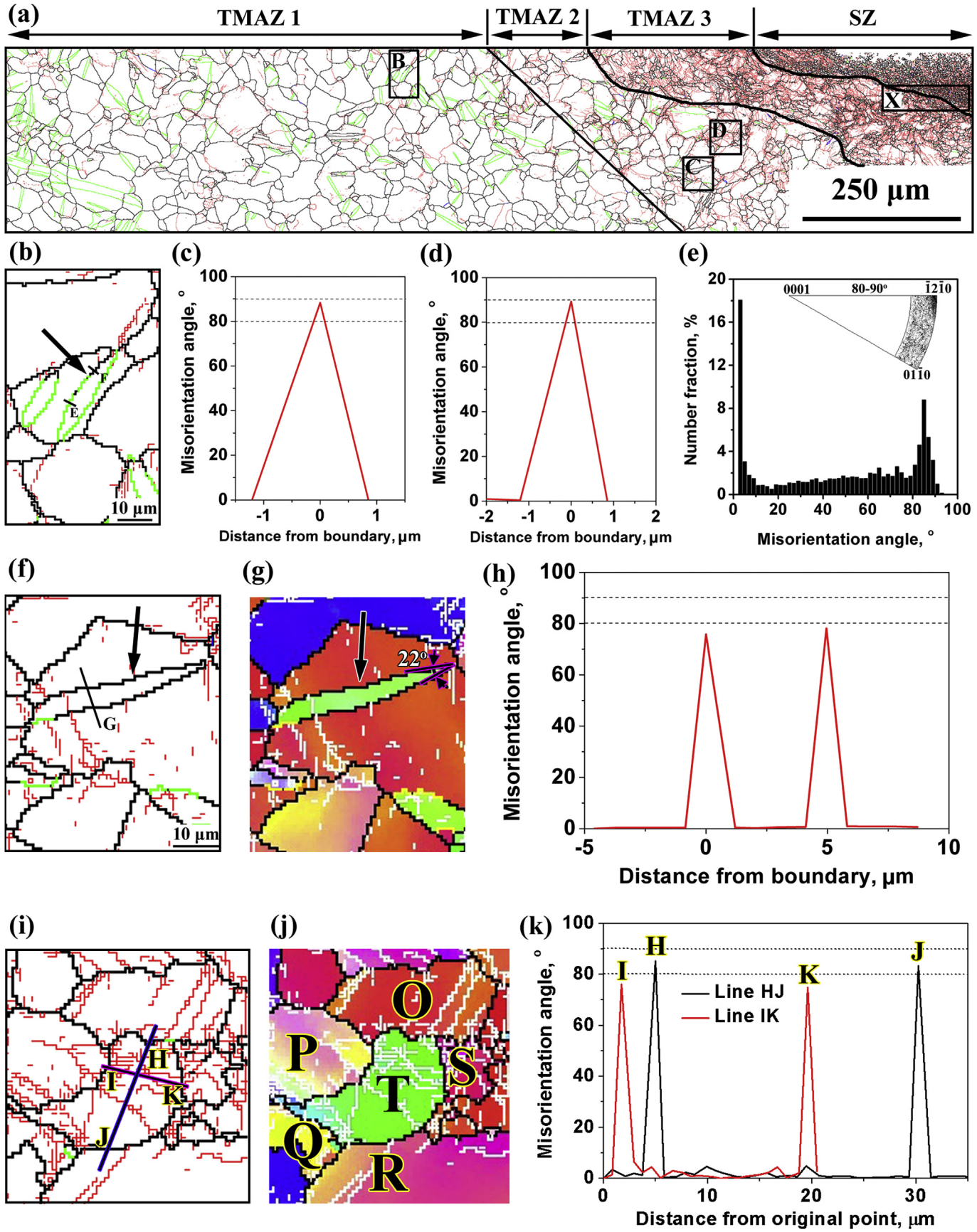

Fig. 3. (a) EBSD of TMAZ and part of SZ in SFS Ti joint; (b) magnified map of rectangle B in TMAZ 1 in (a) showing boundary characteristics, (c) and (d) misorientation distribution along lines E and F in (b); (e) misorientation angle distribution of TMAZ 1; (f) magnified map of rectangle C in TMAZ 2 in (a), (g) orientation map of (f), (h) misorientation distribution along line G in (f); (i) magnified map of rectangle D in TMAZ 2 in (a), (j) orientation map of (i), and (k) misorientation distribution along lines HJ and IK in (i). Black, red and green lines represent HAGBs, LAGBs and $\{10\bar{1}2\}$ TBs, respectively. For the orientation maps in (g) and (j), black, white and yellow lines represent HAGBs, LAGBs and $\{10\bar{1}2\}$ TBs, respectively. (For interpretation of the references to colour in this figure legend, the reader is referred to the Web version of this article.)

Table 2
Fractions of LAGBs, TBs and (sub-)grain sizes in different zones from BM to SZ.

	BM	TMAZ 1	TMAZ 2	TMAZ 3	SZ edge
LAGB,%	23.9	24.4	55.0	67.8	40.2
$\{10\bar{1}2\}$ TB,%	0.6	8.7	2.4	0.2	0.1
HAGB spacing, μm	25.7	21.1	18.7	9.3	2.3
LAGB spacing, μm	24.3	17.4	11.6	2.12	1.16

In TMAZ 3, the fraction of LAGBs further increased to 67.8%, and only 0.2% of the $\{10\bar{1}2\}$ TBs was observed (Fig. 3a and Table 2). In order to reveal the microstructural evolution more clearly, a typical zone, rectangle X in Fig. 3a, is magnified in Fig. 6a. In most cases, a complete boundary consisted of segments of incomplete HAGBs and LAGBs, as shown by arrows in Fig. 6a. The misorientations of the typical incomplete LAGB and HAGB segments are shown in Fig. 6c. When closer to the transition point of LAGBs and HAGBs (lines L1 to L4 in Fig. 6b), the misorientation of the LAGB gradually increased until over 15°, resulting in the formation of the HAGB. Therefore, these HAGB segments were likely transformed from the gradual increase of LAGBs, which is usually associated with CDRX [22,27]. Besides, a small fraction of $\{10\bar{1}1\}$ twins were found (the blue arrow in Fig. 6b). It was reported that $\{10\bar{1}1\}$ twins were usually activated in Ti when the deformation temperature was over 350 °C [12], which suggested that the temperature might exceed 350 °C. In the SZ edge near TMAZ 3, the grains were significantly refined (Figs. 3a and 6a). A lot of boundaries consisted of incomplete HAGBs and LAGBs (arrows in Fig. 6a), just as in TMAZ 3. Therefore, CDRX should be the main grain refinement mechanism in TMAZ 3 and the SZ edge.

The dislocation characteristics in TMAZ 3 are shown in Fig. 7. Most dislocations in TMAZ 3 were determined to be <a> type (not shown here), and they lay on the prismatic plane, as shown in Fig. 7a. According to Fig. 5, these prismatic <a> dislocations mainly exhibited the character of screw type dislocations, and they were arranged into a dislocation wall along the <0002> direction. Besides prismatic <a> dislocations, a small number of <a> dislocations on the basal plane were also observed (Fig. 7b). Therefore, in TMAZ 3, prismatic slip was the main deformation mechanism, with less occurrence of basal slip.

Moreover, in TMAZ 3, a large number of dislocations tangled into dislocation cells (DCs), and dislocations nearby tended to be

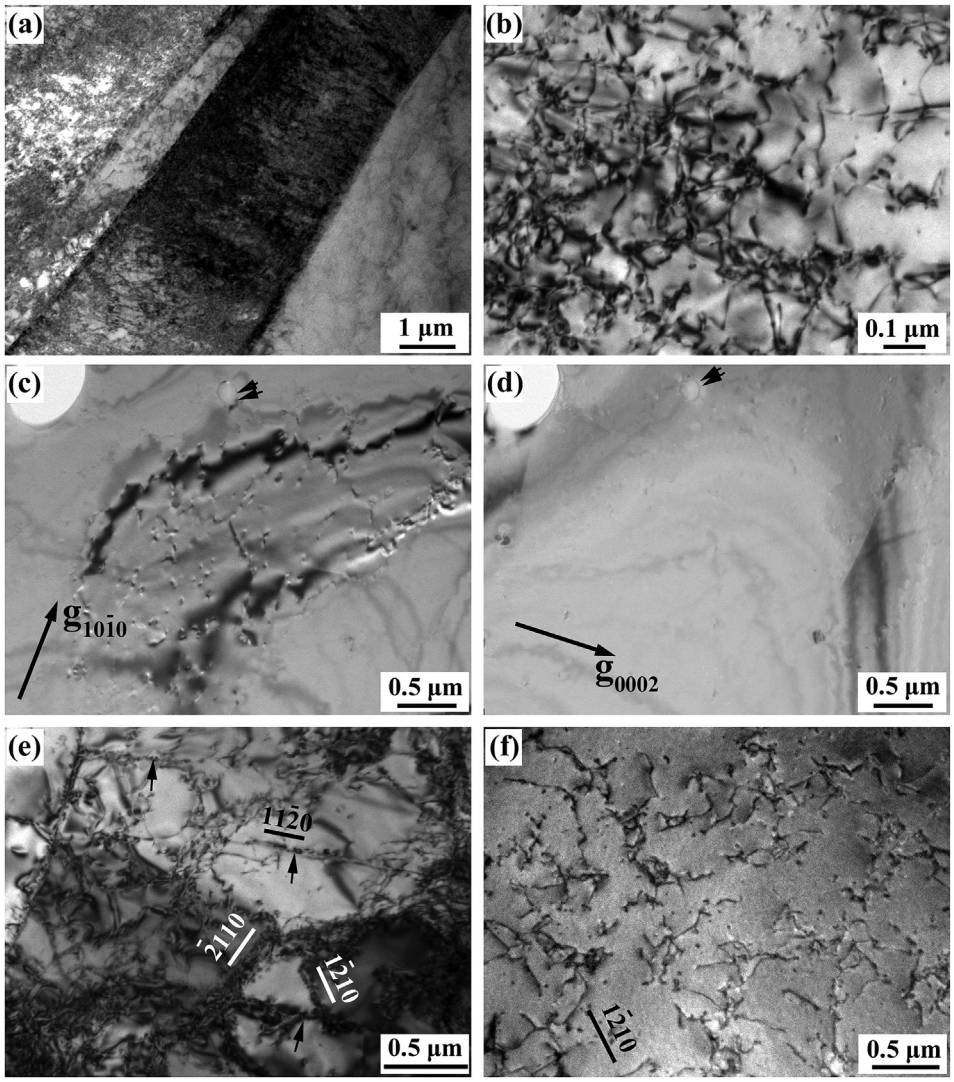

Fig. 4. Typical TEM images of TMAZs 1 and 2 showing (a) twins interacting with dislocations, (b) dislocations within twins, (c) and (d) dislocation characteristics for the same region under $g_{10\bar{1}0}$ and g_{0002} two-beam conditions, respectively. The normal direction of the specimen is near <$1\bar{2}10$> direction. TEM images in (e) and (f) show dislocations in different regions with inclined electron beam slightly deviated from <0002> direction.

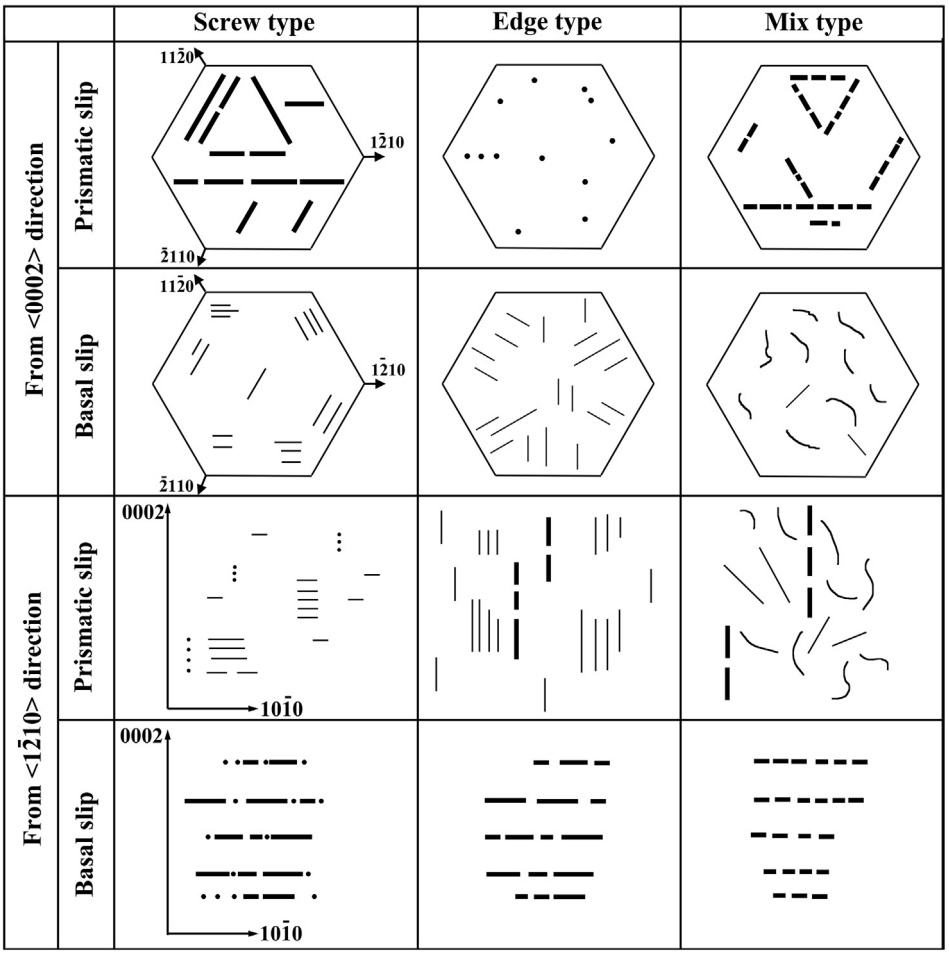

Fig. 5. Schematic of prismatic and basal <a> dislocation characteristics observed from <0002> and <1$\bar{2}$10> direction. Coarse lines represent overlapped effect, and dots indicate dislocation ends resulted from projection.

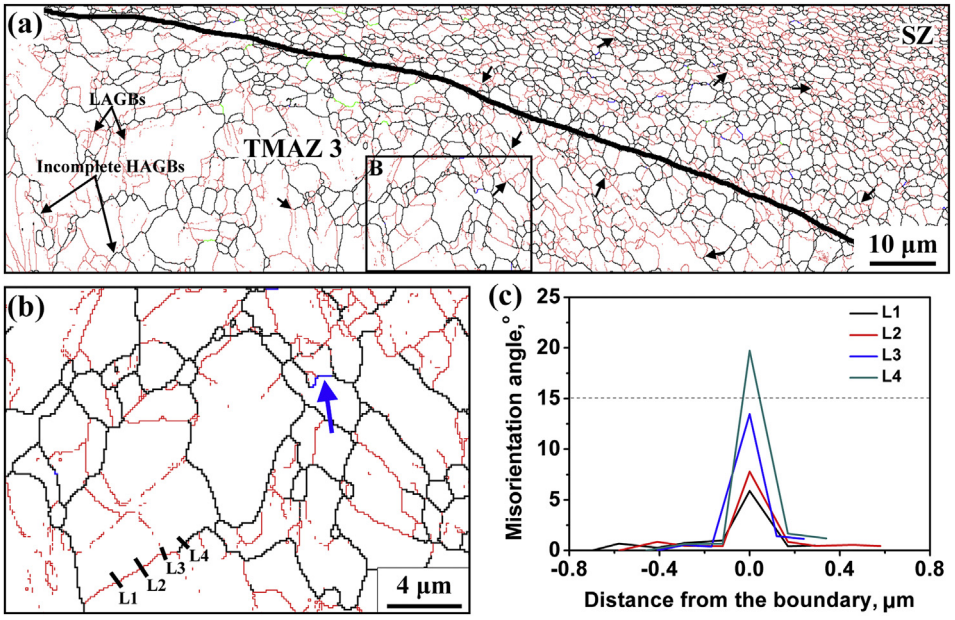

Fig. 6. (a) Magnified EBSD map of rectangle X in Fig. 3a and (b) magnified EBSD map of rectangle B in (a), and (c) misorientation distribution along lines L1, L2, L3 and L4 in (b). Blue lines in (a) and (b) represent {10$\bar{1}$1} TBs. (For interpretation of the references to colour in this figure legend, the reader is referred to the Web version of this article.)

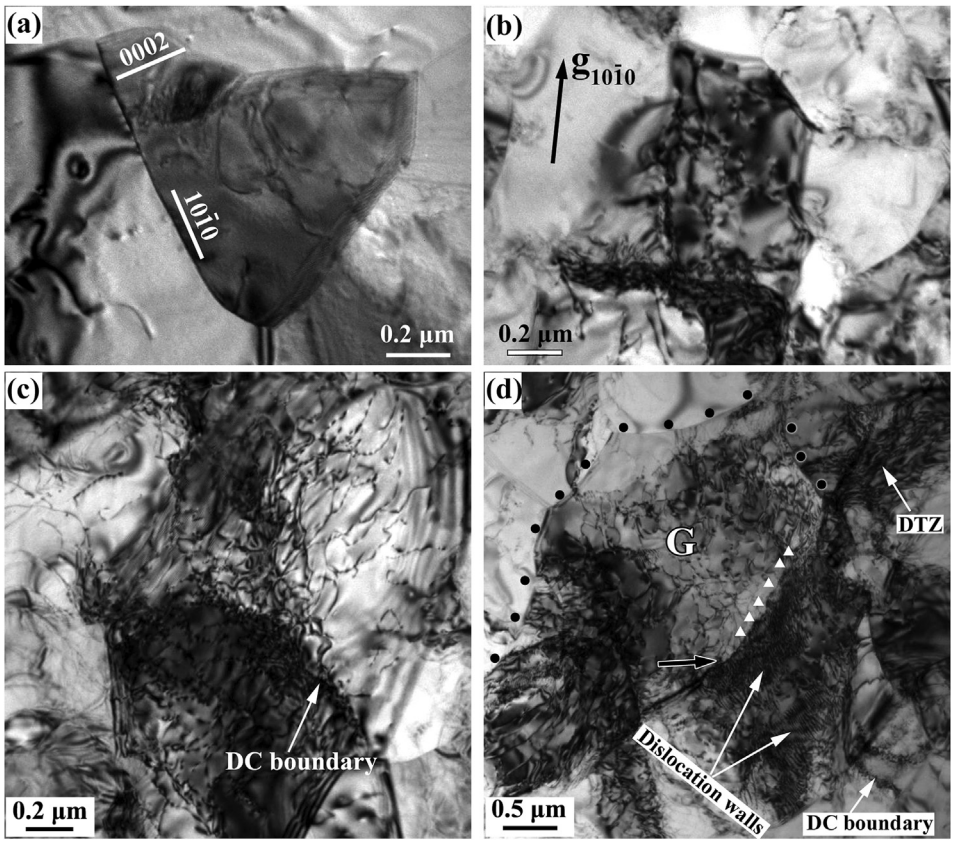

Fig. 7. Dislocation substructure characteristics in TMAZ 3: (a) observed along approximately <1$\bar{2}$10> direction, (b) under $g_{10\bar{1}0}$ two-beam condition, (c) DC boundary, and (d) various substructure morphologies with a typical characteristic with dislocation absorbing.

absorbed into DC boundaries (Fig. 7c). Various substructures including DC boundaries, subgrain boundaries related to dislocation walls, and dislocation tangle zones (DTZs) are identified in Fig. 7d. A typical grain "**G**" is surrounded by segments of grain boundaries (black dots in Fig. 7d) and subgrain boundaries related to dislocation walls (white triangles), agreeing well with the EBSD result (Fig. 6). Also, a large number of dislocations were absorbed continuously into subgrain boundaries formed by dislocation walls (black arrow in Fig. 7d). Thus, CDRX in TMAZ 3 might be related to the dislocation activities, which will be discussed in Section 4.2.

3.3. Stir zone

In the SZ, the material usually experiences a severe plastic deformation (a typical strain ~10–40) [14,28] and DRX, and grain structures in different regions of the SZ might be different, as shown in Fig. 8. The grain distribution in various regions was relatively homogeneous with a significant refinement. In various regions, the phenomenon of LAGBs transforming to HAGBs, i.e. CDRX, was evidently visible (e.g. the arrows in Fig. 8c). Also, a very strong {0002} texture was exhibited in each region, and a typical example in the center SZ with the texture peak near the welding direction is shown in the insert in Fig. 8b. This strong {0002} texture has usually been found in FS α-Ti and Mg alloys [9,10]. Besides, a small fraction of {10$\bar{1}$2} and {10$\bar{1}$1} TBs (green and blue lines) was observed in the ultrafine grains.

Table 3 shows the quantified microstructural characteristics for five different regions of the SZ corresponding to positions 1–5 in Fig. 8. The fractions of {10$\bar{1}$2} and {10$\bar{1}$1} twins were less than 1% in the SZ. An average grain size of <1 μm with a strong texture (>30 times random) was exhibited. One interesting phenomenon was that, in different regions, the grain/subgrain sizes exhibited a similar variation trend with the texture intensity, while the fraction of HAGBs showed a negative correlation with the texture intensity. This phenomenon should be related to texture-induced grain convergence, which was reported in HCP metals during FSW [8,10]. The strong texture means that most grains had a close orientation, and the neighboring grains with a low orientation difference had a strong tendency to converge into large grains with lower misorientation. As a result, the fraction of HAGBs decreased and the grain size increased [10]. It was reported that the fraction of HAGBs saturated was in the range of 60–80% during large deformation when CDRX dominated [29]. In this study, the fraction of HAGBs saturated was just within this range (Table 3), further suggesting that CDRX dominated the grain refinement process in the SZ. Also, the continuous variation of the misorientation angle distribution from TMAZ 2 to the SZ (please refer to Supplementary Fig. S4) was the characteristic of CDRX [27].

Figs. 9a and b show the typical dislocation characteristics in the SZ at the same observation area under the two-beam condition with the inclined beam near the <1$\bar{2}$10> direction. Visible dislocations were arranged into a subgrain boundary (double arrows in Fig. 9a) under the g_{0002} vector, but almost disappeared under the $g_{10\bar{1}0}$ vector (Fig. 9b), which were determined to be <a + c> dislocations. Also, the dislocations in the grain were visible with the $g_{10\bar{1}0}$ vector (Fig. 9b) but invisible with the g_{0002} vector (Fig. 9a), and were determined as the <a> type dislocations. Besides, when the inclined beam was along approximately the <1$\bar{2}$10> direction, most of the <a> dislocations exhibited irregular morphologies and orientations, as shown in Fig. 9b, which indicated that most <a> dislocations lay on the prismatic planes (Fig. 5). Therefore, prismatic <a> and pyramidal <a + c> dislocations were the main

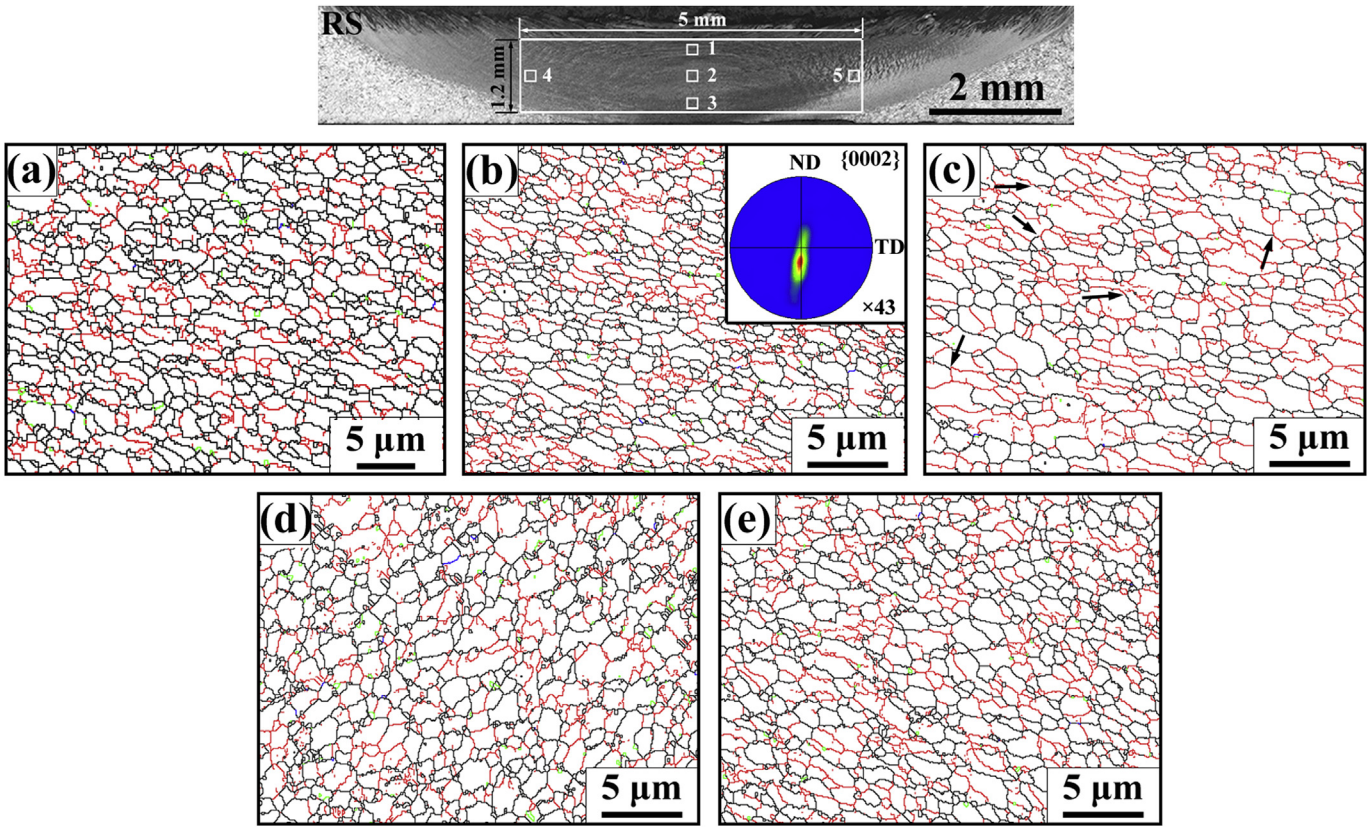

Fig. 8. Microstructure of different regions near SZ center: (a) position 1, (b) position 2 with inserted {0002} pole figure, (c) position 3, (d) position 4, and (e) position 5.

Table 3
(Sub-)grain sizes, texture intensity and fractions of TBs, HAGBs in five regions in SZ corresponding to positions 1–5 in Fig. 8

	Position 1	Position 2	Position 3	Position 4	Position 5	Average
$\{10\bar{1}2\}$ TB, %	0.78	0.61	0.38	1.75	0.72	0.85
$\{10\bar{1}1\}$ TB, %	0.09	0.08	0.04	0.26	0.07	0.11
HAGB spacing, μm	0.68	0.85	1.35	1.06	1.01	0.99
LAGB spacing, μm	0.51	0.59	0.80	0.79	0.70	0.68
{0002} Texture intensity	32	43	58	45	47	45
HAGB, %	70.3	59.7	53.6	65.4	60.2	61.8

deformation mechanism in the SZ.

Fig. 9c shows some nano-sized $\{10\bar{1}1\}$ twins in the ultrafine grains. Besides, there were lots of net-shaped dislocation substructures including a hexagonal network and another network with an angle of 120° (Fig. 9d). These substructures were usually the result of the interaction of <a> dislocations during recovery [30]. Moreover, the phenomenon that a large number of dislocations were continuously absorbed into subgrain boundaries was commonly observed (Fig. 9e), just as in TMAZ 3. Also, a dislocation-free new grain "**F**" migrating into a deformed grain "**G**" was sometimes observed (Fig. 9f), which was the typical grain-bulging feature associated with DDRX nucleation. Therefore, from the TEM and EBSD observations (Figs. 8, 9e and 9f), CDRX was the main grain refinement mechanism, with a limited occurrence of DDRX in the SZ.

3.4. Temperature simulation by finite element method

It is reported that the operation of deformation modes and DRX mechanisms is largely dependent on temperature [12,29]. In order to explain the deformation and DRX mechanisms, the temperature field distribution on the whole SFS joint, and the temperature history of different zones of the joint during SFS were simulated by the finite element method, as shown in Fig. 10. From the 3D temperature distribution in Fig. 10a, the peak welding temperature was 687 °C, which was distributed on the surface of the joint. Fig. 10b shows that the temperature distribution on the cross section. It was obvious that the temperature gradually increased from the BM to the SZ. In this cross-sectional temperature distribution, the borders of different zones of the joint were roughly marked based on the principle as follows.

First, the border of the SZ and the TMAZ was determined (the coarse red line in Fig. 10b) according to their border of the optical cross section in Fig. 1. Thus, the temperature was determined to be over ~400 °C. Second, in TMAZ 3, the formation of $\{10\bar{1}1\}$ twins suggested that the temperature in TMAZ 3 was over 350 °C [12], and thus the isothermal line of 350 °C was approximately regarded as the border of TMAZ 3 and TMAZ 2 (red line in Fig. 10b). Third, in TMAZ 2, a large number of LAGBs were introduced due to great dynamic recovery, which was reported to occur when Ti was

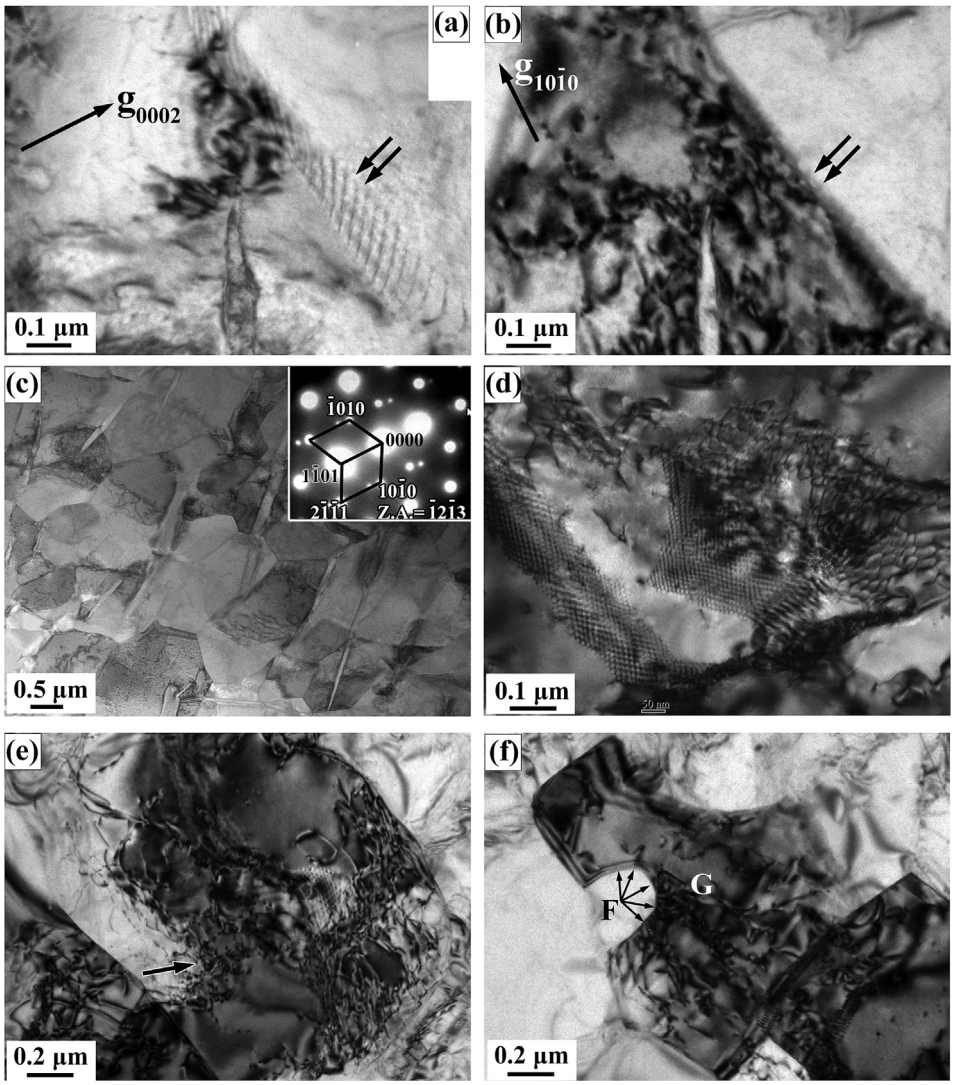

Fig. 9. TEM images reflecting dislocation substructure and DRX characteristics in SZ: dislocation characteristics under (a) g_{0002} and (b) $g_{10\bar{1}0}$ two-beam condition, (c) a typical twinning characteristic with an inserted selected area diffraction, (d) net-shaped dislocation substructures, (e) dislocation absorbing characteristic, and (f) fine grain F growing into large grain G with larger density of dislocations.

deformed at 300–400 °C [11,30]. Thus, the isothermal line of 300 °C was approximately regarded as the border of TMAZ 2 and TMAZ 1 (red line in Fig. 10b).

From the analyses above, the temperature in TMAZ 1, TMAZ 2, TMAZ 3 and the SZ was roughly determined to be < 300 °C, ~300–350 °C, ~350–400 °C, and ~400–687 °C, respectively. It should be pointed out that the border of different zones in the joint was difficult to strictly distinguish, and the subdivision of different zones in Fig. 10b was just an approximate treatment inferred from the microstructure of the corresponding zones.

In order to further understand the influence of the duration time at high temperature on the microstructural evolution, the temperature variation with time for different zones from TMAZ 1 to the SZ (corresponding to Points A-D in Fig. 10b) were predicted, as shown in Fig. 10c. It was obvious that the duration time over 200 °C in TMAZ 1, over 300 °C in TMAZ 2, over 350 °C in TMAZ 3 and over 400 °C in the SZ was ~6.7s, ~10.4s, ~12.8s and ~11.5s, respectively. Thus, the duration time at high temperature for the joint was rather short. More information on the duration time at elevated temperature for the different zones is shown in Table 4. It should be pointed out that in order to verify the feasibility of the simulation method in this study, the temperature at the bottom center of the SZ was also measured by a K-type thermocouple, as shown in Supplementary Fig. S5. The simulated temperature curve agreed well with the measured one, which suggested that the simulated temperature field was reliable in this study, and the detailed description please refer to the text related to Supplementary Fig. S5.

4. Discussion

4.1. Deformation mode

As we know, prismatic slip is usually regarded as the main deformation mode during plastic deformation of α-Ti because of its minimum critical resolved shear stress (CRSS). However, <a> slip cannot accommodate the strain in the <c> direction, and thus cannot provide five independent slip systems for homogeneous plastic deformation in polycrystalline metals. Twinning and <c + a> slip can provide the strain accommodation along the <c> direction and are usually activated during plastic deformation of HCP metals [12].

In this study, besides prismatic slip, basal slips and {10$\bar{1}$2} twins

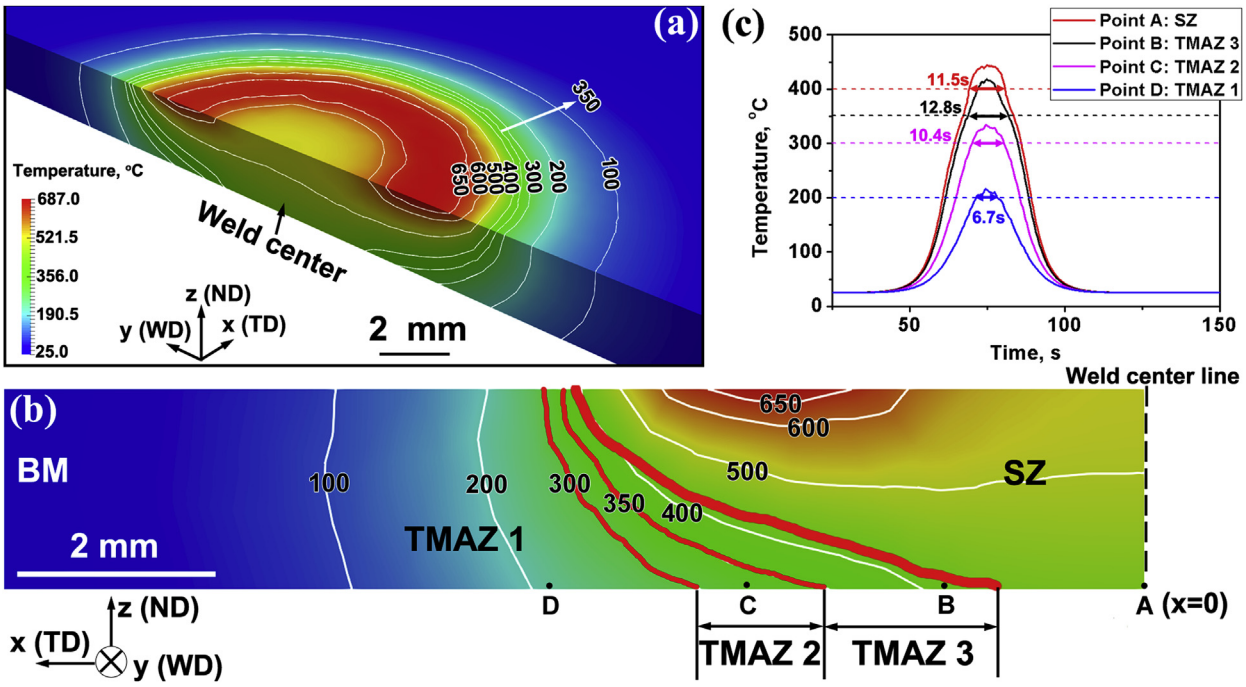

Fig. 10. Temperature field during SFS simulated by finite element method: (a) 3D temperature distribution in joint, (b) temperature distribution (unit: °C) in cross section of SFS joint, and (c) temperature curves of Points A-D in (b) (x = 0, 2, 4 and 6 mm, respectively). The white and red lines in (b) represent the isothermal and the border lines of different zones, respectively. (For interpretation of the references to colour in this figure legend, the reader is referred to the Web version of this article.)

Table 4
Duration time over elevated temperatures of 100–400 °C in different zones from TMAZ 1 to SZ (unit: s). The data were acquired from the temperature curves in Fig. 10c.

	Duration time over elevated temperature, s				
	100 °C	200 °C	300 °C	350 °C	400 °C
TMAZ 1	24.0	6.7	–	–	–
TMAZ 2	31.1	20.5	10.4	–	–
TMAZ 3	35.2	26.5	19.2	12.8	6.0
SZ	36.6	28.7	21.6	16.1	11.5

were the main deformation modes in TMAZs 1 and 2 during SFS (Fig. 4). It has been reported that $\{10\bar{1}2\}$, $\{11\bar{2}1\}$, $\{11\bar{2}2\}$ and $\{10\bar{1}1\}$ twinning is usually involved during plastic deformation of α-Ti, and the $\{10\bar{1}2\}$ twin is the most major twinning system at room temperature due to its low CRSS and small shear strain (s = 0.167) [11]. As a plastic deformation mechanism, one important role of twinning is to accommodate the strain. It was reported that $\{10\bar{1}2\}$ twinning only accounted for <15% of the total plastic strain as a result of the limited relative atomic movement for twinning [11]. It usually occurs at the early deformation stage, but is exhausted under a medium strain [31]. Therefore, one reason for $\{10\bar{1}2\}$ twinning only dominating at TMAZs 1 and 2 was that it was almost exhausted in TMAZ 3, where a typical equivalent plastic strain was ~(5–10) [14,28].

Besides, the occurrence of mechanical twinning strongly relies on the temperature and grain size. It is reported that, similar to dislocation slip, the grain size dependence of the CRSS of twinning also obeys a Hall–Petch relationship, with the slope being one order of magnitude larger [32,33]. Moreover, the CRSS of twinning is insensitive to temperature, but that of dislocation slip decreased rapidly as the temperature increased. In short, coarser grains and lower temperature facilitate twinning. In TMAZs 1 and 2, the duration time at ~200–350 °C was less than 25s, which indicated that the material in these regions could be regarded to experience a warm working for a very short time. Thus, both the relatively low temperature of <~350 °C and coarse grains in TMAZs 1 and 2 promoted twinning. However, closer to the SZ, twinning was largely hindered by both the gradually refined grains and the increased temperature. Actually, the fraction of the TBs started to decrease (Table 2) in TMAZ 2 with a temperature range of ~300–350 °C since great dynamic recovery associated with the dislocation activities took place. In TMAZ 3, the great refined grains and a relatively high temperature of ~350–400 °C significantly hindered twinning, and $\{10\bar{1}2\}$ twins almost disappeared. Therefore, $\{10\bar{1}2\}$ twins only dominated TMAZs 1 and 2 where a small strain, relatively low temperature and coarse grains were exhibited, which accommodated the strain incompatibility, especially along the <c> direction.

Although prismatic slip has its minimum CRSS during plastic deformation of Ti at ambient temperature, the activated slip mode is also affected by the grain orientation and temperature [11,12]. It was reported that mechanical twins were beneficial for the activation of the basal slip [16]. As we know, the slip orientation could be totally changed by rotating the grains, and the soft orientation for prismatic slip could even transform into that for basal slip by rotating ~90° around the $<11\bar{2}0>$ axis [12]. In TMAZs 1 and 2, a large number of $\{10\bar{1}2\}$ twins were activated, and rotated 85° around the $<11\bar{2}0>$ axis of the base grains. Therefore, this probably re-orientated the grains into softer orientations for the basal slip, promoting its occurrence.

In the SZ, besides prismatic slip, pyramidal <c + a> slip was activated. Although the CRSS of pyramidal <c + a> slip is ~3–5 times higher than that of prismatic <a> slip at room temperature [12,32,33], it decreases greatly with the temperature, and it is similar to that of <a> slip above 400 °C [12]. In the SZ, the processing temperature was ~400–687 °C (Fig. 10), which promoted the activation of <c + a> slip. Besides, the strain rate in the SZ could approach an order of 10 s^{-1} [1]. At such a large strain rate with a low thermal conductivity of Ti, an adiabatic heat probably existed,

which further promoted the occurrence of pyramidal <c + a> slip. As we know, the materials in the SZ experienced a typical strain of ~10–40 [14,28]. At such a large strain, a large number of accommodation dislocations must be activated for the strain incompatibility. Especially in the <c> direction, the strain incompatibility was mainly accommodated by <c + a> dislocations.

Moreover, TEM observation shows that many $\{10\bar{1}1\}$ twins were activated in the ultrafine grains in the SZ (Fig. 9c), although their fraction was only 0.11% by EBSD (Table 3), which might be the result of nano-sized twins being too fine to be distinguished by EBSD. $\{10\bar{1}1\}$ twins were usually activated in Ti when the deformation temperature was over 350 °C [12]. In the SZ, the temperature was ~400–687 °C (Fig. 10), which provided a precondition for the formation of $\{10\bar{1}1\}$ twins. Besides, although it is very difficult for twinning in the ultrafine grains because of the greatly increasing CRSS, the large strain rate could greatly promote twinning. In the SZ, a large strain rate with the order of 10 s^{-1} probably induced the activation of $\{10\bar{1}1\}$ twins in the ultrafine grains [1].

4.2. Grain refinement mechanism

In this study, the grain refinement process during SFS was involved with TDRX, CDRX and DDRX, and TDRX dominated at the early deformation. It was reported that TDRX (or"twins" DRX) usually included three steps, i.e. the formation of TBs; their transformation into the random HAGBs by the twin-twin and/or twin-dislocation interaction, or the migration of the TBs; and finally their migration [16,35–38]. Thus, the dynamic nucleation of new grains associated with TDRX could be caused by the twin-twin interaction, twin-dislocation interaction, and/or the migration of TBs [16,35–38]. In this study, the dynamic nucleation of TDRX new grains was mainly related to the interaction of TBs with dislocations, inferred by Figs. 3 and 4a.

According to Figs. 3 and 4a, the detailed grain refinement process in TMAZs 1 and 2 was as follows. At first, the twinning occurred, and then the TBs interacted with the dislocations. As a result, the special orientation relationship of the twins with the base grains was gradually broken, and thus the TBs were completely transformed into "T-HAGBs". At this moment, one original base grain was divided into several new grains. But these new grains were unsteady, because their grain boundary angles were not equilibrium. Hence, these "T-HAGBs" had a strong trend to migrate, in order to form steady grains with equilibrium grain boundary angles. As a result of the migration of the "T-HAGBs", steady new grains were formed. Therefore, the TDRX process took place.

TDRX is reported to play an important role in the grain refinement of HCP alloys, especially for Mg alloys [16,35–38]. For example, Ma et al. [35] found that TDRX took place by the migration of the TBs during the extrusion of Mg alloys at 450 °C. TDRX occurs usually at a relatively high temperature when related to the migration of the TBs, since it is driven by the thermal effect [35]. In this study, the occurrence of TDRX was closely related to the relatively low temperature at the early stage during SFS. In TMAZs 1 and 2 with a relatively low temperature (<350 °C), a large number of dislocations and twins quickly multiplied. Thus, it was very easy to take place for the interaction of the TBs with dislocations, which finally resulted in the occurrence of TDRX. Actually, DRX associated with the interaction of TBs with dislocations has been reported in the surface mechanical attrition treatment of Ti at room temperature [11].

In the past few years, several mechanisms of CDRX have been proposed, such as subgrain rotation associated with grain/phase boundary sliding [22], and the misorientation increase of the subgrain related to dislocation absorption [13]. In this study, CDRX should be related to the misorientation increase of subgrain boundaries by means of the dislocation absorption, which could be inferred from the TEM observations in Figs. 7c, d and 9e. The detailed grain evolution process could be described as follows. At the beginning, a large number of dislocations were introduced into the original grains. As the strain increased, these dislocations tangled into DTZs or DCs. Later, dislocations were absorbed continuously into DTZs or DCs, which were transformed to subgrain boundaries. These subgrain boundaries thereafter repeatedly absorbed dislocations to gradually increase the misorientation, and finally transformed to grain boundaries once reaching a critical value (e.g. 15°). As a result, CDRX took place [27]. Therefore, CDRX in this study was closely related to the dislocation activities.

CDRX and DDRX usually compete with each other, depending on the temperature, strain and original grain state, etc. [29,39]. Generally speaking, DDRX takes place when new grains dynamically form through the pre-existing grain boundary bulging, followed by a long-distance boundary migration. Thus, DDRX usually occurs at high temperature where the boundary mobility becomes high. However, CDRX involves short-distance migration of atoms, and thus the effect of temperature on CDRX was weaker than that on DDRX [39]. Besides, CDRX involves the formation of new grains by the gradual increase of the misorientaion of LAGBs. Since recovery consumes stored energy, if LAGBs need to further increase their misorientation to turn into HAGBs, more deformation energy is needed. In other words, a larger deformation benefits CDRX. Also, at relatively low temperatures, dislocations can multiply rapidly, which is beneficial for CDRX with a dislocation absorption mechanism. Therefore, the choice of DRX mechanisms depends on a critical temperature and strain that drive the bulging and migration of grain boundaries or the further increase of the misorientation of the recovery subgrains [39].

In TMAZ 3, CDRX related to dislocation absorption took place for the following reasons. First, in TMAZ 3, a large strain (~5–10 [14,28]) could provide enough deformation energy for CDRX. Second, it was reported that during large plastic deformation of Mg alloys, CDRX took place at a medium temperature range where cross-slip controlled the deformation rate [34]. As we know, a higher SFE and screw dislocations can promote the occurrence of cross-slip. A high SFE of >300 mJ/m^3 for Ti and most screw dislocations in TMAZ 3 (Fig. 7a) were both beneficial for cross-slip, thereby benefiting CDRX. Moreover, during SFS, the excessive heat could be taken away by the flowing water in time. As a result, a medium temperature of ~350–400 °C was exhibited in TMAZ 3 (Fig. 10), which further enhanced the occurrence of CDRX.

In the SZ, CDRX dominated the deformation, but limited DDRX also occurred. It was reported that the nucleation and growth of recrystallized nuclei occurred when annealing after rolling of Ti at 400–600 °C [11]. The temperature in the SZ was 400–687 °C, and such a high temperature was of benefit to DDRX nucleation. On the other hand, from the viewpoint of slip systems, compared with only the <a> slip systems activated, the activation of both <a> and <a + c> slips in the SZ (Fig. 8) increased the microstructural heterogeneity within the grains, which might increase the orientation gradient, thereby increasing the possibility of DDRX. However, considering the competition of CDRX and DDRX, as the deformation temperature and strain changed, the operation of DRX mechanisms might change, and there was a critical temperature and strain for CDRX transition into DDRX. As the strain increased, the transition temperature increased. In other words, CDRX would take place at a higher temperature when the strain increased [39]. In the SZ, due to the typical large strain of ~10–40 [14,28], the transition temperature from CDRX to DDRX greatly increased. As a result, CDRX even dominated at the high temperature range of 400–687 °C.

Furthermore, it is reported that when nucleation of DDRX occurs by a bulging mechanism, the critical condition would be [30].

$$\frac{\rho_m^3}{\dot{\varepsilon}} > \frac{2\gamma_b}{KLMGb^5} \quad (6)$$

$\dot{\varepsilon}$ represents the strain rate. K and G are constant and the Gibbs free energy, respectively. M and γ_b are the boundary mobility and the grain boundary energy, respectively. ρ_m, L and b represent the density of free dislocations, the mean slip distance of dislocations and the Burgers vector of dislocations, respectively.

The terms on the right hand in Equation (6) could be regarded as approximately constant at a particular temperature [30], and thus when $\frac{\rho_m^3}{\dot{\varepsilon}}$ achieves a critical value, the DDRX nucleation takes place. This means that, besides the boundary mobility (M), the density of free dislocations and strain rate are also key factors influencing the operation of DDRX. The possibility of the operation of DDRX increases when the free-dislocation density increases or the strain rate decreases. In the SZ, although the temperature was high, which resulted in a high boundary mobility, the large strain rate with an order of 10 s^{-1} probably decreased the chance of DDRX. Besides, although the SZ experienced a severe plastic deformation, which led to a large dislocation density, most of the dislocations were trapped in the subgrain boundaries by recovery, such as the net-shaped substructures in Fig. 9d. As a result, the density of free dislocations greatly decreased, which also reduced the possibility of DDRX. Besides, DDRX is related to long range diffusion, and a relatively long time at high temperature is usually needed for DDRX to occur. In the SZ, the duration time over 400 °C was only <12s (Fig. 10c). It was very likely that there was not enough time for the occurrence of DDRX at high temperature for such a short duration, which also reduced the extent of DDRX. Therefore, based on the discussion above, the medium temperature, large strain and strain rate increased the chance of the operation of CDRX.

4.3. Dynamic equilibrium of grain refinement and coarsening

In order to more accurately clarify the extent of grain refinement in different regions, we defined a similar grain refinement factor as ECAP [40], that is

$$\eta = (d_0\text{-}d_1)/d_0 \quad (7)$$

where η represents the grain refinement efficiency, d_0 is the original grain size before refinement, and d_1 is the new grain size after refinement.

Table 5 shows the grain refinement efficiency for different deformation zones. The grain refinement efficiency in TMAZs 1 and 2 dominated by TDRX was relatively small, not more than 20%, while for the zones dominated by CDRX, the grain refinement efficiency greatly increased, and the maximum grain refinement efficiency of 75% occurred in the SZ edge. This means that CDRX, rather than TDRX, contributed to the main grain refinement in the whole SFS process. Entering the SZ, the grain refinement efficiency greatly decreased, with only 19.8% in the SZ center. This suggested that there must be grain coarsening mechanisms to reduce the extent of grain refinement, thereby reaching a dynamic equilibrium with the grain refinement process in the SZ.

As mentioned above, in the SZ, grains were refined mainly by dislocations absorption (Figs. 7c, d and 9c). Supposing that this process by dislocation absorption was always repeated, grains would be refined approaching to zero, only if there was a large enough strain. However, in the practical case, the grain could not be refined without limits, and the grains size will tend to a certain steady value (e.g. ~1 μm) when the strain reaches a certain large value (e.g. ~10) [27]. This should be attributed to the fact that dynamic grain boundary migration (GBM) driven by deformation is not negligible. It was reported that the driving force of the GBM came from the local dislocation density differences, and the GBM rate increased rapidly with the strain rate, even with a power law function for Al [27]. In the SZ with a large strain rate of the order of 10 s^{-1}, a large GBM rate must exist. As a result, a dynamic equilibrium would be achieved between the GBM process and CDRX process in the SZ with a typical strain of ~10–40 [14,28].

Besides, the SZ showed a very strong texture of >30 times random (Table 3). Under such a strong texture, the convergence of neighboring grains would easily take place, resulting in grain coarsening, which facilitated a reduction of the extent of grain refinement. Therefore, the ultrafine grain in the SZ should be the result of the dynamic balance between the grain refinement process dominated by CDRX and the grain coarsening process, including deformation-induced GBM and texture-induced grain convergence.

4.4. Schematic of deformation and grain refinement mechanisms during SFS

Based on the analysis and discussion above, the deformation and grain refinement mechanisms during SFS are summarized in Fig. 11. At the beginning of deformation, an abundance of twins with prismatic and basal <a> dislocations were activated, which divided the original grains into finer twin regions (Fig. 11b). Later, twins interacted with <a> dislocations, which resulted in the transition of TBs into random HAGBs (Fig. 11c). Twin regions were gradually evolved into new grains. As the temperature increased, the twin activity largely decreased until it almost disappeared, and the dislocation activity dominated the grain refinement process. At this stage, prismatic slip dominated the deformation, with less occurrence of basal slip. After a rapid multiplication of <a> dislocations, they were rearranged into subgrain boundaries (Fig. 11d). These subgrain boundaries increased their misorientation by continuous dislocation absorption, and finally transformed into HAGBs, i.e. the CDRX process (Fig. 11e). At the final stage, when the temperature rose above ~400 °C, both prismatic <a> and pyramidal <a + c> slips occurred. In addition to CDRX with dislocation absorption, limited DDRX concurrently took place, further refining the grains (Fig. 11f). Besides, grain coarsening took place by means of dynamic GBM and texture-induced grain convergence, and reached a dynamic balance with CDRX and limited DDRX. As a result, the uniform ultrafine grains formed in the SZ, where the temperature, strain and strain rate were the largest (Fig. 11g). As mentioned in Section 4.2, the large strain and strain rate with medium temperature promoted CDRX. As we know, uniform fine recrystallized grains can be obtained by CDRX. Therefore, this study

Table 5
Grain refinement efficiency in different zones.

	TMAZ 1	TMAZ 2	TMAZ 3	SZ edge	RS-SZ (Position 4 in Fig. 8)	Center-SZ (Position 2 in Fig. 8)
Grain refinement efficiency, %	17.9	11.1	50.3	75.3	53.9	19.8

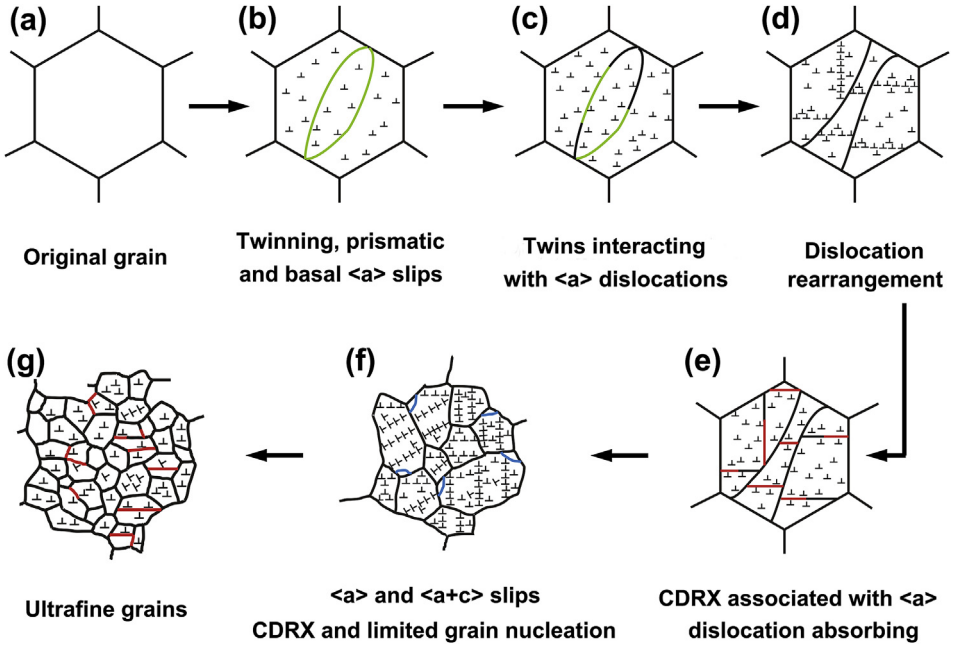

Fig. 11. Schematic of deformation and grain refinement process during SFS of pure Ti. Black, green, red and blue lines represent HAGBs, TBs, LAGBs and grain nucleation, respectively. (For interpretation of the references to colour in this figure legend, the reader is referred to the Web version of this article.)

provides a way to design uniform ultrafine structures by decreasing the temperature and increasing the strain and strain rate.

5. Conclusions

Commercially pure titanium was subjected to SFS under water for the first time and a defect-free joint with a joint efficiency of 100% was successfully produced, showing the feasibility of SFS for Ti-based materials. The initial coarse-grained microstructure gradually evolved into an ultrafine one, which was mainly attributed to various DRX mechanisms accompanied by deformation modes with three stages. At the beginning, deformation was mainly controlled by $\{10\bar{1}2\}$ twinning, prismatic and basal slips. The grain refinement mechanism was TDRX related to the interaction of $\{10\bar{1}2\}$ twins with <a> dislocations. As the temperature increased over ~350 °C, prismatic slip dominated the deformation, with less occurrence of basal slip, and the grain refinement mechanism changed to CDRX associated with dislocation absorption. When the temperature rose above ~400 °C, prismatic slip and pyramidal <a + c> slip were the main deformation mechanisms. The ultrafine grain structure was the result of the dynamic balance of the grain refinement process dominated by CDRX and limited DDRX, and the grain coarsening process induced by the large strain and the strong texture.

Acknowledgements

This work was supported by the National Natural Science Foundation of China under Grant Nos. 51601194, 51471171 and 51331008, and the IMR SYNL-T.S. Kê Research Fellowship.

Appendix A. Supplementary data

Supplementary data to this article can be found online at https://doi.org/10.1016/j.actamat.2018.12.059.

References

[1] R.S. Mishra, Z.Y. Ma, Friction stir welding and processing, Mater. Sci. Eng. R 50 (2005) 1–78.
[2] P. Xue, D.R. Ni, D. Wang, B.L. Xiao, Z.Y. Ma, Effect of friction stir welding parameters on microstructure and mechanical properties of the dissimilar Al-Cu joints, Mater. Sci. Eng., A 528 (2011) 4683–4689.
[3] L.H. Wu, K. Nagatsuka, K. Nakata, Achieving superior mechanical properties in friction lap joints of copper to carbon-fiber-reinforced plastic by tool offsetting, J. Mater. Sci. Technol. 34 (2018) 1628–1637.
[4] M.A. Mofid, A. Abdollah-Zadeh, F.M. Ghaini, C.H. Gur, Submerged friction-stir welding (SFS) underwater and under Liquid Nitrogen: an improved method to join Al Alloys to Mg alloys, Metall. Mater. Trans. 43A (2012) 5106–5114.
[5] L.H. Wu, H. Zhang, X.H. Zeng, P. Xue, B.L. Xiao, Z.Y. Ma, Achieving superior low temperature and high strain rate superplasticity in submerged friction stir welded Ti-6Al-4V alloy, Sci. China Mater. 61 (2018) 417–423.
[6] P. Xue, B.L. Xiao, Q. Zhang, Z.Y. Ma, Achieving friction stir welded pure copper joints with nearly equal strength to the parent metal via additional rapid cooling, Scripta Mater. 64 (2011) 1051–1054.
[7] J.Q. Su, T.W. Nelson, C.J. Sterling, Friction stir processing of large-area bulk UFG aluminum alloys, Scripta Mater. 52 (2005) 135–140.
[8] S. Mironov, U.F.H.R. Suhuddin, Y.S. Sato, H. Kokawa, C.W. Lee, Grain structure evolution during friction-stir welding of AZ31 magnesium alloy, Acta Mater. 57 (2009) 5406–5418.
[9] S. Mironov, T. Onuma, Y.S. Sato, H. Kokawa, Microstructure evolution during friction-stir welding of AZ31 magnesium alloy, Acta Mater. 100 (2015) 301–312.
[10] S. Mironov, Y.S. Sato, H. Kokawa, Development of grain structure during friction stir welding of pure titanium, Acta Mater. 57 (2009) 4519–4528.
[11] K.Y. Zhu, A. Vassel, F. Brisset, K. Lu, J. Lu, Nanostructure formation mechanism of alpha-titanium using SMAT, Acta Mater. 52 (2004) 4101–4110.
[12] D.H. Shin, I. Kim, J. Kim, Y.S. Kim, S.L. Semiatin, Microstructure development during equal-channel angular pressing of titanium, Acta Mater. 51 (2003) 983–996.
[13] J.Q. Su, T.W. Nelson, R. Mishra, M. Mahoney, Microstructural investigation friction stir welded 7050-T651 aluminium, Acta Mater. 51 (2003) 713–729.
[14] P.B. Prangnell, C.P. Heason, Grain structure formation during friction stir welding observed by the 'stop action technique, Acta Mater. 53 (2005) 3179–3192.
[15] S. Mironov, Y.S. Sato, H. Kokawa, H. Inoue, S. Tsuge, Structural response of superaustenitic stainless steel to friction stir welding, Acta Mater. 59 (2011) 5472–5481.
[16] A.H. Feng, Z.Y. Ma, Microstructural evolution of cast Mg-Al-Zn during friction stir processing and subsequent aging, Acta Mater. 57 (2009) 4248–4260.
[17] A.L. Pilchak, J.C. Williams, Microstructure and texture evolution during friction stir processing of fully lamellar Ti-6Al-4V, Metall. Mater. Trans. 42A (2011) 773–794.
[18] L.H. Wu, D. Wang, B.L. Xiao, Z.Y. Ma, Tool wear and its effect on microstructure

and properties of friction stir processed Ti-6Al-4V, Mater. Chem. Phys. 146 (2014) 512–522.
[19] L.H. Wu, P. Xue, B.L. Xiao, Z.Y. Ma, Achieving superior low-temperature superplasticity for lamellar microstructure in nugget of a friction stir welded Ti-6Al-4V joint, Scripta Mater. 122 (2016) 26–30.
[20] K.E. Knipling, R.W. Fonda, Microstructural evolution in Ti-5111 friction stir welds, Metall. Mater. Trans. 42A (2011) 2312–2322.
[21] L.H. Wu, B.L. Xiao, D.R. Ni, Z.Y. Ma, X.H. Li, M.J. Fu, Y.S. Zeng, Achieving superior superplasticity from lamellar microstructure of a nugget in a friction-stir-welded Ti–6Al–4V joint, Scripta Mater. 98 (2015) 44–47.
[22] L.H. Wu, D. Wang, B.L. Xiao, Z.Y. Ma, Microstructural evolution of the thermo-mechanically affected zone in a Ti-6Al-4V friction stir welded joint, Scripta Mater. 78–79 (2014) 17–20.
[23] X.X. Zhang, B.L. Xiao, Z.Y. Ma, A transient thermal model for friction stir weld. Part I: the model, Metall. Mater. Trans. A 42A (2011) 3218–3228.
[24] R. Nandan, G.G. Roy, T.J. Lienert, T. Debroy, Three-dimensional heat and material flow during friction stir welding of mild steel, Acta Mater. 55 (2007) 883–895.
[25] X.X. Zhang, D. Wang, B.L. Xiao, H. Andrae, W.M. Gan, M. Hofmann, Z.Y. Ma, Enhanced multiscale modeling of macroscopic and microscopic residual stresses evolution during multi-thermo-mechanical processes, Mater. Des. 115 (2017) 364–378.
[26] D.R. Chichili, K.T. Ramesh, K.J. Hemker, The high-strain-rate response of alpha-titanium: experiments, deformation mechanisms and modeling, Acta Mater. 46 (1998) 1025–1043.
[27] S. Gourdet, F. Montheillet, A model of continuous dynamic recrystallization, Acta Mater. 51 (2003) 2685–2699.
[28] X.M. Deng, S.M. Xu, A study of texture patterns in friction stir welds, Acta Mater. 56 (2008) 1326–1341.
[29] H. Jazaeri, F.J. Humphreys, The transition from discontinuous to continuous recrystallization in some aluminium alloys I – the deformed state, Acta Mater. 52 (2004) 3239–3250.
[30] F.J. Humphreys, M. Hatherly, RECRYSTALLIZATION and Related Annealing Phenomena, second ed., Elsevier, Oxford, 2003.
[31] Z.P. Zeng, S. Jonsson, H.J. Roven, The effects of deformation conditions on microstructure and texture of commercially pure Ti, Acta Mater. 57 (2009) 5822–5833.
[32] K.D. Molodov, T. Al-Samman, D.A. Molodov, G. Gottstein, On the role of anomalous twinning in the plasticity of magnesium, Acta Mater. 103 (2016) 711–723.
[33] J.C. Gong, A.J. Wilkinson, A microcantilever investigation of size effect, solid-solution strengthening and second-phase strengthening for < a > prism slip in alpha-Ti, Acta Mater. 59 (2011) 5970–5981.
[34] A. Galiyev, R. Kaibyshev, G. Gottstein, Correlation of plastic deformation and dynamic recrystallization in magnesium alloy Zk60, Acta Mater. 49 (2001) 1199–1207.
[35] Q. Ma, B. Li, E.B. Martin, S.J. Horstemeyer, Twinning-induced dynamic recrystallization in a magnesium alloy extruded at 450 ^{o}C, Scripta Mater. 65 (2011) 823–826.
[36] O. Sitdikov, R. Kaibyshev, T. Sakai, Dynamic recrystallization based on twinning in coarse-grained Mg, Mater. Sci. Forum 419–422 (2003) 521–526.
[37] J. Peng, Z. Zhang, Y. Li, W. Zhou, Y. Wu, Twinning-induced dynamic recrystallization and micro-plastic mechanism during hot-rolling process of a magnesium alloy, Mater. Sci. Eng., A 699 (2017) 99–105.
[38] M.G. Jiang, H. Yan, R.S. Chen, Twinning, recrystallization and texture development during multidirectional impact forging in an AZ61 Mg alloy, J. Alloy. Comp. 650 (2015) 399–409.
[39] N. Dudova, A. Belyakov, T. Sakai, R. Kaibyshev, Dynamic recrystallization mechanisms operating in a Ni-20%Cr alloy under hot-to-warm working, Acta Mater. 58 (2010) 3624–3632.
[40] Y.J. Chen, Y.J. Li, J.C. Walmsley, S. Dumoulin, S.S. Gireesh, S. Armada, P.C. Skaret, H.J. Roven, Quantitative analysis of grain refinement in titanium during equal channel angular pressing, Scripta Mater. 64 (2011) 904–907.